An electrochemistry-based impedance model for lithium-ion batteries

Shengbo Eben Li [b], Baojin Wang [a,c,*], Huei Peng [a], Xiaosong Hu [a]

[a] *Department of Mechanical Engineering, The University of Michigan, Ann Arbor, MI 48109, USA*
[b] *State Key Lab of Automotive Safety and Energy, Department of Automotive Engineering, Tsinghua University, Beijing 100084, China*
[c] *Department of Control Science and Engineering, Harbin Institute of Technology, Harbin, 150001, China*

HIGHLIGHTS

- An electrochemistry-based impedance model for lithium-ion batteries is proposed.
- An optimization method is used to identify the model parameters from EIS data.
- The accuracy of the proposed model is compared with that of the Randles model.
- Some parameters of the proposed model show clear trend with aging cycles.

ARTICLE INFO

ABSTRACT

Accurate models of lithium-ion batteries are important for analyzing and predicting battery dynamics and aging. This paper presents an electrochemistry-based impedance model for lithium-ion batteries to better understand the relationship between battery internal dynamics and external measurement. The proposed impedance model is a modified single particle model which balances between simplicity and accuracy. The model includes electrochemical impedance due to charge-transfer reaction, diffusion dynamics in the electrodes, effects of ion concentration, capacitance dispersion in the double layer, and anode insulating film growth, etc. The impedance tests for model validation were performed on two lithium-ion cells at ambient temperature and at different SOC levels. A particle swarm optimization method is employed to identify model parameters. The model accuracy under different conditions is compared with that of conventional Randles model and the parameter variations at different stage of the aging process are studied.

© 2014 Elsevier B.V. All rights reserved.

1. Introduction

Lithium-ion batteries are promising energy storage devices for portable electronics, electrified vehicles and renewable energy storage [1 2]. The prediction of battery performances is important, especially for highly dynamic applications, e.g. electrified vehicles and grid storage systems [3,4]. In the past decades considerable efforts have been made to analyze, model and control battery behaviors, including open-circuit potential, charging/discharging dynamics, capacity loss, etc. [5–8]. The electrochemical impedance spectroscopy (EIS) method has been used to characterize the battery impedance behavior over a wide frequency range [5,9]. It is also recognized to have the ability to distinguish different physical processes inside batteries and determine their process rates by non-destructive measurements [10]. When using EIS, a properly

designed battery impedance model is needed. This impedance model is expected to depict battery internal dynamics, including charge-transfer reaction on electrode/electrolyte interface, lithium-ion diffusion in electrodes, double layer effects, and the resistance/capacitance growth of the anode insulating film, etc. [11].

Many earlier impedance models are equivalent circuit typed because of their simple form [12]. The most classic one is the Randles model, which includes a Warburg element, a resistor and a RC circuit. The common understanding is that the Warburg element represents diffusion dynamics, the resistor represents pure ohmic resistance, while the RC component represents the double layer effects. The Randles model and its variants have been used to estimate state of health (SOH), e.g. Waag et al. [13], Eddahech et al. [14] and Mukoyama et al. [7]. One main disadvantage is that it is not easy to directly relate internal physical properties of batteries to model prediction. This disadvantage has limited the application of this type of models on designing high-performance battery management systems and battery designs.

* Corresponding author. Tel: +1 734 615 3084; fax: +1 734 757 3563.
 E-mail addresses: baojin.wang@live.com, baojin.w@gmail.com (B. Wang).

Significant work has been published on electrochemistry-based impedance expression. Meyers et al. first proposed an impedance model for a single particle and then extended it for electrodes with porous structure [15]. The modeled dynamics include the charge-transfer reaction, double layer effect and solid-phase diffusion. The particle-size distribution is considered to accurately describe the solid-phase diffusion. This model ignored the electrolyte diffusion limitations for simplicity, which might limit its application to high current charging/discharging conditions. In addition, it is assumed in Meyers's study that there is only one phase in electrode, however, some researchers argued that certain types of lithium-ion batteries may have multiple phases, e.g. Andersson et al. [16,17]. For two-phase particles, Huang et al. developed a semi-mathematical impedance model by combining electrochemical components and equivalent circuit components [18]. Huang's model considers two homogenous phases, which is better suited for lithium iron phosphate (LFP) batteries. Sikha et al. further considered the diffusion process in electrolyte when modeling an insertion cathode/separator/foil anode cell [19]. This work is also extended to a dual insertion electrode battery, in which the insertion electrodes are separated by an ionic conductive membrane [20]. Abraham et al. developed an electrochemical model to fit the impedance data of $LiNi_{0.8}Co_{0.15}Al_{0.05}O_2$-based positive electrodes, in which the diffusion dynamics in electrolyte, solid−electrolyte interface (SEI) and active-material surface layer was considered [21]. These electrochemistry-based impedance models can describe battery internal dynamics such as ion diffusion and migration in electrodes and electrolyte, charge-transfer reaction on the electrode/electrolyte interface, etc. However, the relatively complex structure and large number of parameters are major challenge in practical battery management systems. As far as we know, only a few models have been used on some narrow topics, e.g., how to study and predict the aging effect [5]. In addition, direct and quantitative relationship between electrochemistry and impedance models is not well established because some important electrochemical features have been neglected, including electrode porosity and the variation of ion concentration. Bridging this gap will help to understand battery dynamics and design a more efficient and effective energy storage system.

The main purpose of this paper is to derive a structurally concise but accurate battery impedance model that directly relates electrochemical and physical parameters with battery internal dynamics. This paper focuses on lithium-ion batteries, beginning with the well-known single particle assumption followed by enhancements for better tradeoff between accuracy and simplicity. The remainder of this paper is structured as follows: Section 2 discusses the structural simplification for lithium-ion batteries. In Section 3, an electrochemistry-based impedance model is derived. Section 4 describes the EIS experiments used for model validation, followed by to the methodology used for model parameter identification. In Section 5, the battery aging effect is discussed using identified parameters at different stage of aging. Section 6 concludes this paper.

2. Simplified battery electrode model

This paper focuses on batteries with lithium oxide based cathode and lithium-carbon based anode. In such batteries, the charge-transfer reaction happens on the electrode/electrolyte interface. During discharging, the lithium-ions de-intercalate from anode, move through the electrolyte, and intercalate into cathode. When charging, the process is reversed. To tradeoff between accuracy and conciseness, it is assumed that (1) electrodes consist of multiple spherical particles, and all particles have identical size and dynamics, (2) the material inside each particle is spatially homogeneous, (3) electrodes have perfect conductivity, i.e., no voltage drop inside a particle or among particles, (4) the SEI film growth caused by aging only happens on the anode surface, (5) the electrolyte, separator and current collectors are treated as lumped pure resistors. With these assumptions each electrode is represented by one lumped spherical particle, shown in Fig. 1.

In addition to diffusion dynamics inside electrode, charge-transfer reaction and double layer effect, which are frequently considered, we consider the following behaviors in our model.

(1) The relationship of lithium-ion concentration and the open-circuit potential: the lithium-ion concentration fluctuates when charging and discharging, which leads to variations in electrochemical potential and overall battery open-circuit potential. The open-circuit potential is often empirically fitted as a mathematical function of SOC, e.g. linear function [15], higher-order polynomials [19,20], etc. These functions do not relate to battery dynamics and provide no insight to electrochemical dynamics. We choose to use the Nernst equation directly to bridge this gap from the viewpoint of thermodynamics.

(2) The capacitance dispersion caused by the porosity of electrodes: both electrodes at present are porous to increase the effective surface area. This porosity leads to battery impedance much more complicated than any commonly used equivalent circuit models. In theory, the porous electrodes can be approximated by multiple spherical particles with predefined size distribution. This approximation, however, often causes unacceptable difficulty in model structure and parameter identification. Here, a constant phase element (CPE) component will be used to describe the capacitance dispersion in the double layer effect [9].

(3) The SEI film growth at anode during degradation: the SEI film growth is a major mechanism of battery degradation. The film growth reduces cyclable lithium-ions and increases internal resistance, which leads to both capacity loss and power fade which is an irreversible side reaction, especially on the anode side [22,23]. This paper ignores the SEI film growth on the cathode side because of its lower significance [24].

Fig. 2 sketches the current flow during discharging for both anode and cathode. The current flow at cathode is similar to that of anode, just without the components related to the SEI film.

In Fig. 2, $J_{FD,i}$ represents the Faradaic current density due to charge-transfer reactions, $Z_{FD,i}$ is the Faradaic impedance of electrodes caused by charge-transfer reactions ($i = n$ for anode and $i = p$ for cathode), determined from the Faradaic current density and the potential across the interface, $\phi_{1,i}$, $\phi_{2,i}$ represent the potential on the two sides of electrode/electrolyte interface, $J_{dl,i}$ represents the double layer current density, $C_{dl,i}$ represents the double layer capacitance, C_{film} represents the capacitance due to the SEI
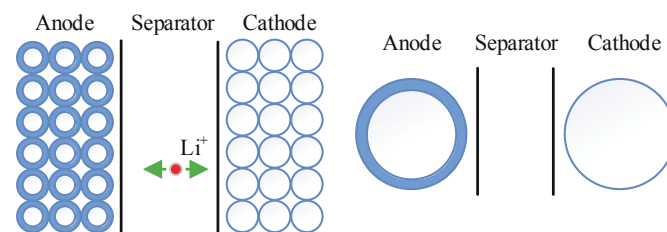

Fig. 1. Simplification of lithium-ion battery electrodes (left − multiple particle; right − single particle).
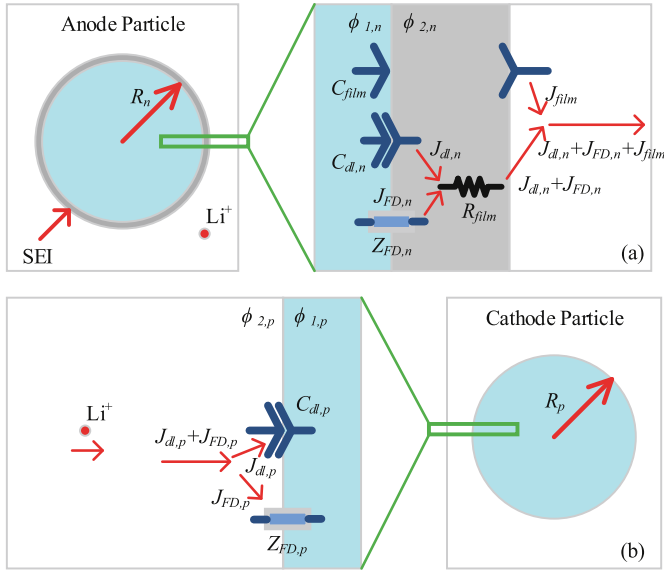
Fig. 2. Current flows at the anode and cathode ((a) anode; and (b) cathode).

film insulation on anode, J_{film} is the current density through the SEI film, and R_{film} is the SEI film resistance. In general, the impedance spectrum of lithium-ion batteries includes multiple sections, for instance, a straight tail at low frequency, a semi-circle at middle frequency and a quarter-circle at high frequency. Detailed discussion will be in Section 4.

3. Battery impedance model

This section first reviews the partial differential equations (PDEs) used to depict battery electrochemical dynamics, including charge-transfer dynamics, open-circuit potential and ion diffusion dynamics in the electrodes. Then, we derive the Faradaic impedance from the well-known Butler–Volmer equation, Nernst equation and Fick's second law, followed by impedance models for anode and cathode. The overall battery impedance is obtained by adding other components, including the double layer capacitance, the SEI film impedance and the pure inductance.

3.1. PDEs for the single particle model

3.1.1. Electrochemical dynamics on electrode surface

The Faradaic current density is governed by the well-known Butler–Volmer equation, which describes the relationship between the overpotential and Faradaic current density, expressed as

$$J_{FD,i} = J_{0,i}\left[\exp\left(\frac{\alpha F}{RT}\eta_i\right) - \exp\left(-\frac{(1-\alpha)F}{RT}\eta_i\right)\right], \quad i = n, p, \tag{1}$$

where η_i is the overpotential, α is the transfer coefficient ($\alpha = 0.5$ as given in Ref. [25]), $J_{0,i}$ is the exchange current density in the nominal condition, F is the Faraday's constant, R is the universal gas constant and T is the absolute temperature. In normal charging and discharging conditions, $J_{0,i}$ is not a constant, but depends on the lithium-ion concentration in the electrodes and electrolyte. In the EIS analysis, the battery is excited with a low amplitude current and therefore $J_{0,i}$ is approximately constant [15]. The overpotential η_i is defined as

$$\eta_i = \phi_{1,i} - \phi_{2,i} - E_i, \quad i = n, p, \tag{2}$$

where E_i is the open-circuit potential of anode and cathode. Here, we use an expression derived from the Nernst equation instead of linear functions or higher-order polynomials, which is more suitable to describe battery inherent mechanism while maintaining a concise structure [26]

$$E_i = E_{0,i} - \frac{RT}{F}\ln\frac{\chi_i}{(1-\chi_i)}, \quad i = n, p, \tag{3}$$

where $E_{0,i}$ is the reference open-circuit potential, χ_i is the mole fraction of the lithium-intercalated sites in the electrodes. The mole fraction is defined as

$$\chi_i = V_i\overline{C}_{1,i}/a_i, \quad i = n, p, \tag{4}$$

where $\overline{C}_{1,i}$ is the average lithium-ion concentration of electrodes, V_i is the electrode volume, and a_i is the maximum mole number of lithium-ions in the electrodes. V_i is often assumed to be constant when a relatively small alternative perturbation is applied in EIS measurement [27]. Let

$$k_i = V_i/a_i, \quad i = n, p, \tag{5}$$

and substitute Eqs. (4) and (5) into Eq. (3), we have

$$E_i = E_{0,i} - \frac{RT}{F}\ln\frac{k_i\overline{C}_{1,i}}{1 - k_i\overline{C}_{1,i}}, \quad i = n, p. \tag{6}$$

In Eq. (6), further information is required to determine the average lithium-ion concentration of electrodes. The average lithium-ion concentration inside a particle is almost equal to that on the surface when battery current is close to zero [28]. Therefore, a relationship between electrode overpotential and bulk ion concentration can be built. In EIS tests, the current applied is relatively small and a similar assumption can be used in the following model derivation.

3.1.2. Diffusion dynamics at anode and cathode

The lithium-ion concentration in both electrode and electrolyte is affected by the ion diffusion dynamics. When modeling, the diffusion in electrolyte is much faster than that in electrode and thus is neglected. The diffusion of lithium-ions in electrodes is governed by the Fick's second law [29]

$$\frac{\partial C_{1,i}}{\partial t} = \frac{D_{1,i}}{r_i^2}\frac{\partial}{\partial r_i}\left(r_i^2\frac{\partial C_{1,i}}{\partial r_i}\right), \quad i = n, p, \tag{7}$$

where r_i is the radial position in the spherical coordinate, $C_{1,i}$ denotes lithium-ion concentration in the particles at radius r_i and time t, $D_{1,i}$ is the diffusion coefficient. The boundary conditions are

$$\left.\frac{\partial C_{1,i}}{\partial r_i}\right|_{r_i=0} = 0, \quad i = n, p, \tag{8}$$

$$\left.\frac{\partial C_{1,i}}{\partial r_i}\right|_{r_i=R_i} = -\frac{J_{FD,i}}{D_{1,i}F}, \quad i = n, p. \tag{9}$$

The boundary conditions of Eq. (8) are because spherical particles are radially symmetric and Eq. (9) is from the mass and charge conversion at the solid–electrolyte interface. It is reasonable to ignore the electrolyte diffusion dynamics when the charge and discharge rate is low because of the higher diffusivity in the electrolyte [25,30]. This condition holds true for our EIS tests.

3.2. Derivation of Faradaic impedance

The diffusion dynamics in the electrodes are described by partial differential equations (PDEs). The PDEs are rewritten into ordinary differential equations (ODEs) using the Laplace transformation method. In the EIS tests, the battery is excited by a small sinusoidal signal and all battery dynamics works in linear regions around equilibrium points. Hence, it is assumed that both the changes of lithium-ion concentration and Faradaic current density fluctuates periodically at the same frequency

$$
\begin{aligned}
J_{\mathrm{FD},i} &= \bar{J}_{\mathrm{FD},i} + \tilde{J}_{\mathrm{FD},i} e^{j\omega t} \\
C_{1,i}(r,t) &= \bar{C}_{1,i} + \tilde{C}_{1,i}(r) e^{j\omega t}
\end{aligned}, \quad i = p,n.
\tag{10}
$$

where variables with a "bar" represents the nominal values and variables with a "tilde" represent the amplitude of perturbation, ω is the excitation frequency. Plugging Eq. (10) to Eq. (7), we have

$$
j\omega \tilde{C}_{1,i} = \frac{D_{1,i}}{r_i^2} \frac{\partial}{\partial r_i}\left(r_i^2 \frac{\partial \tilde{C}_{1,i}}{\partial r_i} \right), \quad i = p,n.
\tag{11}
$$

Now Eq. (11) becomes a nonlinear second order ODE. Solving Eq. (11) together with the associated boundary conditions Eqs. (8) and (9), we obtain the lithium-ion concentration on the surface of particles ($r_i = R_i$)

$$
\begin{aligned}
\tilde{C}_{1,s,i} &= \tilde{C}_{1,i}(R_i) = \psi_{1,i}\tilde{J}_{\mathrm{FD},i} \\
\psi_{1,i} &= -\frac{R_i}{\mathrm{FD}_1\left(R_i\sqrt{\frac{j\omega}{D_1}}\cdot\coth\left(\sqrt{\frac{j\omega}{D_1}}R_i\right)-1 \right)}
\end{aligned}, \quad i = n,p.
\tag{12}
$$

In the following, we use $C_{1,s,i}$ to denote the lithium-ion concentration on the surface of particles. Substituting Eq. (6) into the linearized Butler–Volmer equation, we have

$$
J_{\mathrm{FD},i} = J_{0,i}\frac{F}{RT}\left(\phi_{12,i} - E_{0,i} + \frac{RT}{F}\ln\frac{k_i C_{1,s,i}}{1-k_i C_{1,s,i}} \right), \quad i = n,p,
\tag{13}
$$

where $\phi_{12,i} = \phi_{1,i} - \phi_{2,i}$. Differentiating Eq. (13),

$$
\Delta J_{FD,i} = J_{0,i}\frac{F}{RT}\Delta\phi_{12,i} + J_{0,i}\frac{1}{C_{1,s,i}(1-k_i C_{1,s,i})}\Delta C_{1,s,i}, \quad i = n,p.
\tag{14}
$$

When excited by a small sinusoidal signal, the variations of all variables in Eq. (14) are also sinusoidal. Hence, we have

$$
\begin{aligned}
\Delta J_{\mathrm{FD},i} &= J_{\mathrm{FD},i} - \bar{J}_{\mathrm{FD},i} = \tilde{J}_{\mathrm{FD},i}e^{j\omega t} \\
\Delta C_{1,s,i} &= C_{1,s,i} - \bar{C}_{1,i} = \tilde{C}_{1,s,i}e^{j\omega t}, \quad i = n,p. \\
\Delta\phi_{12} &= \phi_{12} - \bar{\phi}_{12} = \tilde{\phi}_{12}e^{j\omega t}
\end{aligned}
\tag{15}
$$

Substitute Eqs. (12) and (15) into Eq. (14), we have

$$
\tilde{J}_{\mathrm{FD},i} = \frac{J_{0,i}F}{RT}\tilde{\phi}_{12} + \frac{J_{0,i}}{C_{1,s,i}(1-k_i C_{1,s,i})}\psi_{1,i}\tilde{J}_{\mathrm{FD},i}, \quad i = n,p.
\tag{16}
$$

The Faradaic impedance of unit surface area is then expressed as

$$
Z_{\mathrm{FD},i} = \frac{\Delta\phi_{12,i}}{\Delta J_{\mathrm{FD},i}} = \frac{RT}{F}\left(\frac{1}{J_{0,i}} + \frac{1}{C_{1,s,i}(1-k_i C_{1,s,i})}\frac{R_i}{\mathrm{FD}_1\left(R_i\sqrt{\frac{j\omega}{D_1}}\cdot\coth\left(R_i\sqrt{\frac{j\omega}{D_1}} \right)-1 \right)} \right),
$$
$$
i = p,n
\tag{17}
$$

Several parameters in Eq. (17), namely, $C_{1,s,i}$, R_i, $D_{1,i}$ and k_i are coupled and cannot be identified separately. Hence, we define two lumped parameters

$$
\begin{aligned}
K_{1,i} &= C_{1,s,i}D_{1,i}F(1 - k_i C_{1,s,i})/R_i, \quad i = n,p. \\
K_{2,i} &= R_i/\left(\sqrt{D_{1,i}}\right)
\end{aligned}
\tag{18}
$$

Then the Faradaic impedance of unit surface area is then expressed as

$$
Z_{\mathrm{FD},i} = \frac{\Delta\phi_{12,i}}{\Delta J_{\mathrm{FD},i}} = \frac{RT}{F}\left(\frac{1}{J_{0,i}} + \frac{1}{K_{1,i}\left(\sqrt{j\omega K_{2,i}^2}\cdot\coth\left(\sqrt{j\omega K_{2,i}^2}\right)-1 \right)} \right),
$$
$$
i = n,p.
\tag{19}
$$

The Faradaic impedance has two items, charge-transfer resistance and the impedance caused by solid-phase diffusion. The charge-transfer resistance is a critical parameter in the battery behavioral analysis. Let $R_{\mathrm{ct},i}$ denote the charge-transfer resistance of unit surface area, expressed as

$$
R_{\mathrm{ct},i} = RT/\left(J_{0,i}F\right), \quad i = p,n.
\tag{20}
$$

The overall Faradaic impedance is related to the surface area. The following model identification process will identify the whole Faradaic impedance, rather than that per unit surface area.

3.3. Derivation of electrode impedance

Besides the Faradaic impedance, the electrode impedance includes the effects of double layer and SEI film (the cathode SEI film impedance is assumed to be zero in this paper). We will lump them together and derive the impedance model for cathode and anode.

3.3.1. Cathode impedance per unit area
Fig. 2(b) shows the current flows in the cathode. The schematic diagram of its equivalent circuit structure is shown in Fig. 3.

The porous electrodes have rough electrode surface which lead to double layer effect with capacitance dispersion, rather than behaving like an ideal capacitor [31]. A constant phase element (CPE) is used to describe this dispersed capacitance [9], expressed as

$$
Z_{\mathrm{dl},i} = 1/\left(C_{\mathrm{dl},i}^0 (j\omega)^{v_i} \right), \quad i = p,n,
\tag{21}
$$

where $Z_{\mathrm{dl},i}$ is the impedance of the CPE, v_i is the exponent to describe the dispersion effect ($0 < v_i \leq 1$). When $v_i = 1$, CPE becomes an ideal capacitor. Combined with Eq. (21), the cathode impedance of unit area is

$$
Z_{\mathrm{p}} = Z_{\mathrm{FD,p}}/\left(1 + Z_{\mathrm{FD,p}}C_{\mathrm{dl,p}}^0 (j\omega)^{v_{\mathrm{p}}} \right).
\tag{22}
$$

3.3.2. Anode impedance of unit area
The anode particle has more complicated equivalent structure as shown in Fig. 4. The CPE is used for both double layer capacitance and SEI film. Here we assume that the SEI film grows
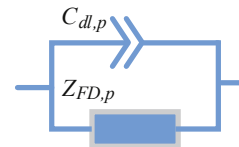
Fig. 3. Cathode equivalent circuit structure.

uniformly over the porous electrode, as a result of which, the CPE representing SEI film impedance has the same exponent as anode double layer capacitance. The anode impedance of unit area, $Z_{n,SEI}$ is expressed as

$$Z_{n,SEI} = \frac{Z_n + R_{film}}{1 + (j\omega)^{\upsilon_n} C_{film}^0 \left(Z_n + R_{film}\right)}, \tag{23}$$

where R_{film} is the resistance of SEI film, and C_{film}^0 is a capacitance-like parameter.

3.4. Full battery impedance model

Fig. 5 shows the model structure of the whole battery. The model structure has an anode impedance and a cathode impedance connected in series. The impedance of electrolyte, separator, and current collector are represented by a pure ohmic resistor R_0, placed between anode and cathode. At high frequency, battery current collectors and cables introduce inductance, which appears as a positive imaginary part in the EIS diagram. This inductive effect is represented by a pure inductor L in Fig. 5.

The overall impedance of a battery $Z_{battery}$ then has the following form:

$$Z_{battery} = j\omega L + Z_{n,SEI}/S_n + R_0 + Z_p/S_p, \tag{24}$$

where S_p and S_n are the cathode and anode effective surface area, respectively.

4. Impedance measurement and parameter identification

4.1. Experiment setup and EIS tests

The EIS measurement was conducted in a battery impedance tester, which has two channels, capable of measuring two cells simultaneously. The two battery cells are lithium-ion typed. Its specifications are listed in Table 1.

The impedance tests are carried out for two cells (noted as A and B) at ambient temperature (25 °C) and two SOC levels (half charged SOC ∼50% and fully charged SOC ∼100%). Fig. 6 shows the impedance measurement of both Cell A and Cell B. The solid lines represent different aging cycles, 200, 400, 600, 800 and 900.

The measured impedance contains three parts: a straight tail at low frequency, a large semi-circle at middle frequency, and a small quarter-circle at high frequency. The general understanding is that the straight tail relates to the diffusion dynamics of lithium-ions in electrodes, the larger semi-circle at middle frequency is associated with the interfacial charge-transfer reaction combined with double layer capacitance, and the quarter-circle at high frequency is due to the presence of SEI film and the particle-to-particle contact of active materials [13].

The aging cycles have a direct influence on the shape and amplitude of impedance. It is observed that as battery degrades,
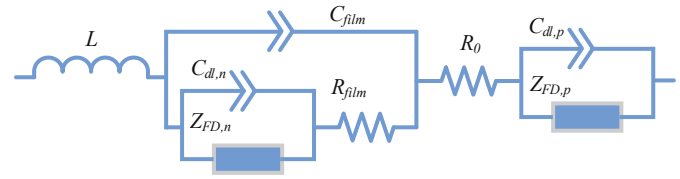

Fig. 5. The overall impedance model of the battery.

the impedance curve gradually shifts rightward and the semi-circle at middle frequency enlarges with the increasing cycle number, and the enlarging semi-circle swallows the straight tail at low frequency. This is an obvious index to show the increase of Faradaic impedance and the slowdown of interfacial charge-transfer reaction. The state of charge also affects the shape and amplitude of impedance. It is observed that the impedance of half charged batteries is smaller than that of the fully charged batteries.

4.2. Model parameter identification

The above-derived impedance model has 16 parameters, listed in Tables 2 and 3, respectively. These parameters are closely related to battery physical and electrochemical characteristics. An identification method is used to minimize the error between impedance measurement and model prediction. The cost function to be optimized is

$$\min_{\widehat{\theta}} \; e = \sum_{f=f_{min}}^{f_{max}} \left(Z_{exp}(f) - Z_{battery}\left(f, \widehat{\theta}\right)\right)^2, \tag{25}$$

where $\widehat{\theta}$ is the estimated parameter set, e is the model error, Z_{exp} is the measured data and f is the frequency point. The Hybrid Multiple Particle Swarm Optimization method (HMPSO) [32] is used to obtain the optimal parameters. The HMPSO is a global optimization method with effective memory utilization, more robust for noisy data and more efficient in maintaining diverse set of search candidates. The effectiveness has been demonstrated in battery equivalent circuit model studies [33].

Before running the optimal parameter identification, we reduced the over-fitting problem by fixing some parameters which are less sensitive to battery SOC and aging. The fixed parameters are listed in Table 2. The reasons to fix these 6 parameters are explained below. According to [5], $C_{dl,p}^0$, $C_{dl,n}^0$ and S_p, S_n are not sensitive to model error and are regarded as constant. We also decide to fix $K_{1,n}$ and L based on the observation of the identification results. The sensitivity analysis by varying these two parameters showed less effect on model fitness than other parameters, moreover, fixing these two parameters helps to avoid over-fitting. Such difficult parameters have been explained by Tröltzsch [5]. The values of S_p and S_n are selected based on known average values of electrode surface areas. The values of $C_{dl,p}^0$, $C_{dl,n}^0$ $K_{1,n}$ and L are determined from results of all aging cycles.
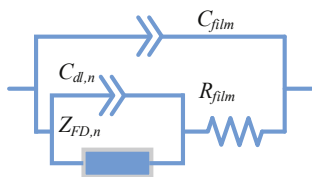

Fig. 4. Anode equivalent circuit structure.

Table 1
Specifications of lithium-ion battery cells.

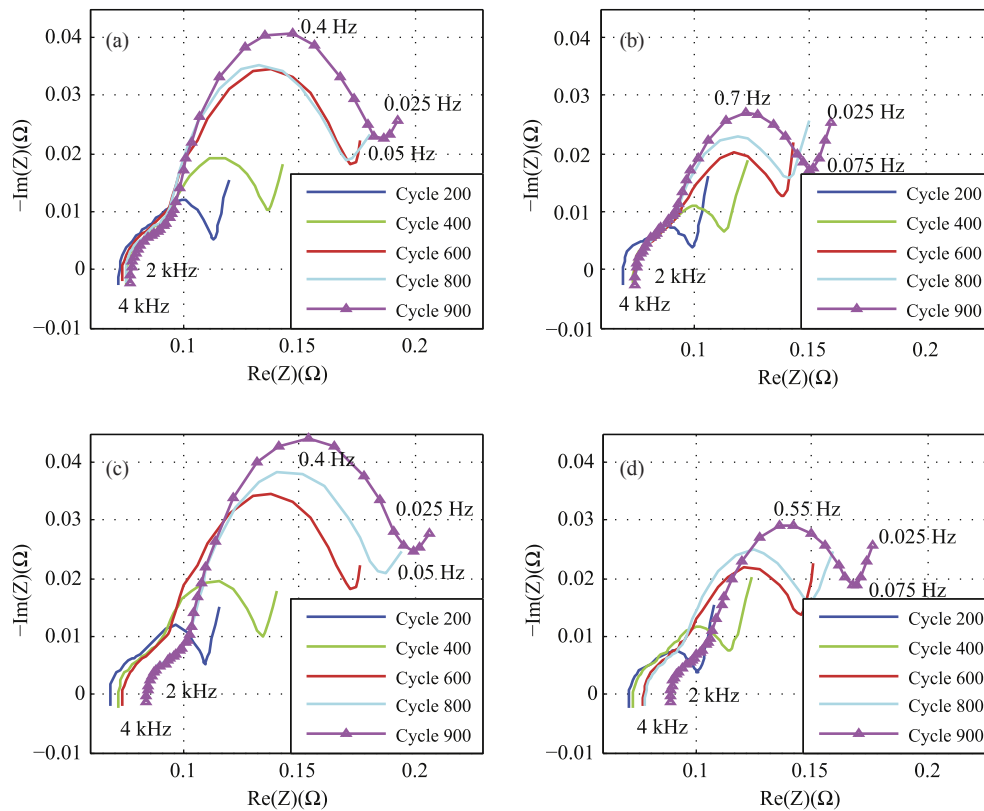| Variable	Value
Capacity	940 mAh
Nominal voltage	3.7 V
Max. voltage	4.2 V
Min. voltage	2.5 V
Energy density	133 Wh kg^{-1}

Fig. 6. Measured impedance under different SOC and aging cycles ((a) Cell A − fully charged; (b) Cell A − half charged; (c) Cell B − fully charged; and (d) Cell B − half charged).

Table 2
Fixed parameters.

No.	Parameters	Description	Value	Unit
1	$C_{dl,p}^0$	Cathode double layer capacitance	7.88	F s$^{v_p-1}$ m^{-2}
2	$C_{dl,n}^0$	Anode double layer capacitance	1.98	F s$^{v_n-1}$ m^{-2}
3	S_p	Cathode effective surface area	3.52	m^2
4	S_n	Anode effective surface area	2.16	m^2
5	$K_{1,n}$	Lumped parameter of anode	1.63	A m^{-2}
6	L	Pure inductor	1.7e−07	H

4.3. Model accuracy analysis

The Randles model is selected to be the baseline for comparison. Figs. 7 and 8 illustrate the fitting results of two models (Randles model and our proposed electrochemistry-based impedance model). Figs. 9 and 10 compare their accuracy based on root mean square error (RMSE) using both Cell A and Cell B data.

Here, we will discuss where the Randles model loses accuracy and how an electrochemistry-based model makes improvement. It is observed from the identification results that the Randles model

loses accuracy in all three frequency range. In the low frequency, the Randles model is bound to have a 45 degree tail, but actual EIS data have a slope higher than 45 degree. We think this is because ion diffusion in the electrodes is in spherical structure and is not along a single dimension. The latter is the assumption of Warburg element used in the Randles model. In the middle frequency, the Randles model predicts the impedance to be a semi-circle, which is different from what actual EIS data look like. The main reason is the capacitance dispersion due to the porosity of electrodes. In the electrochemistry-based model, the CPE component can describe this frequency-dependent characteristic, which demonstrates the importance of considering electrode porosity. The Randles model loses the ability to depict high frequency impedance because it omits some impedance components. The model accuracy on average is 0.65 mΩ (RMSE, root mean square error) for the proposed model, about one-eighth that of the Randles model.

5. Parametric variation due to aging

It is apparent that battery impedance changes significantly with aging. The impedance curve gradually shifts rightward and the semi-circle at the middle frequency region enlarges with the battery age. We identified the battery parameters of the proposed electrochemistry-based model with the abovementioned EIS data. The identified parameters of two cells are averaged at the same SOC and aging cycle in order to reduce the uncertainties of cell inconsistency. Table 4 lists the average critical parameters of fully charged state (at different aging cycles: 200, 400, 600, 800 and 900), while Table 5 lists those of half charged state (at different aging cycles: 200, 400, 600, 800 and 900).

Fig. 11 shows the relationship between pure ohmic resistance and aging cycles. Some researchers believed that the pure ohmic

Table 3
Free parameters.

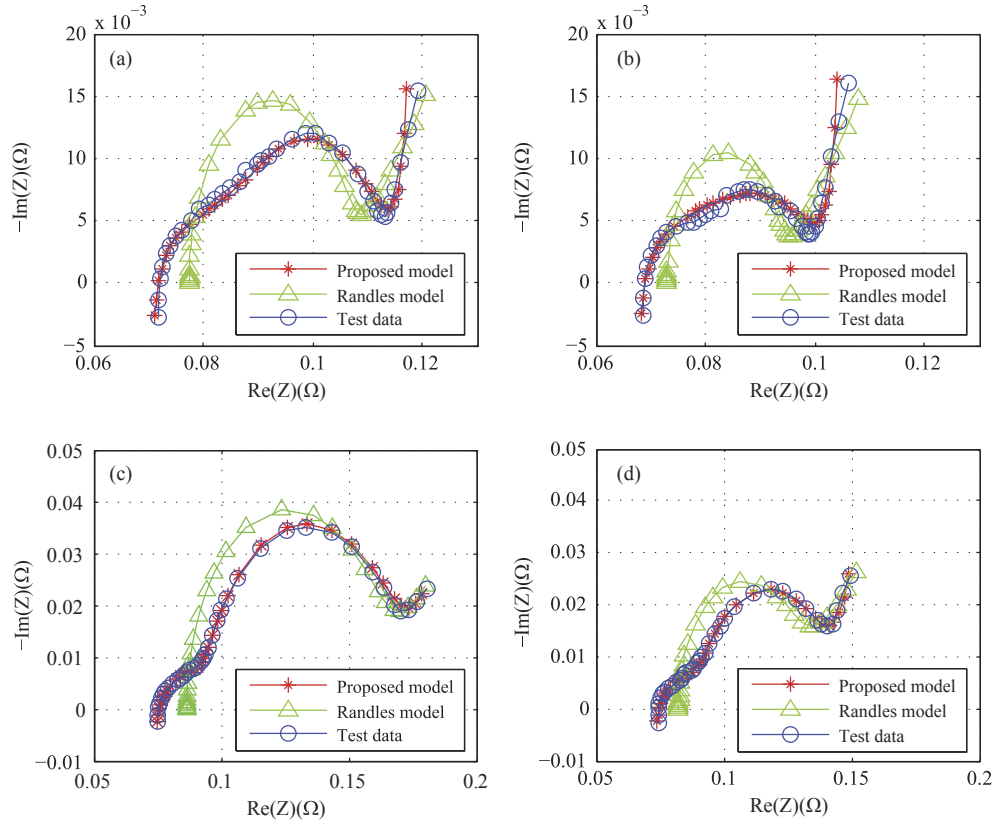| No.	Parameters	Description	Unit
7,8	$J_{0,i}$, $i = p,n$,	Exchange current density	A m^{-2}
9	$K_{1,p}$	Lumped parameter of cathode	A m^{-2}
10,11	$K_{2,i}$, $i = p,n$,	Lumped parameter of electrodes	s$^{0.5}$
12,13	v_i, $i = p,n$,	Exponent of CPE element	–
14	R_{film}	SEI film resistance	Ω m^2
15	C_{film}^0	SEI film capacitance	F s$^{v_n-1}$ m^{-2}
16	R_0	Pure resistance	Ω

Fig. 7. Fitting results of battery impedance (Cell A) ((a) Cycle 200, fully charged; (b) Cycle 200, half charged; (c) Cycle 800, fully charged; and(d) Cycle 800, half charged).
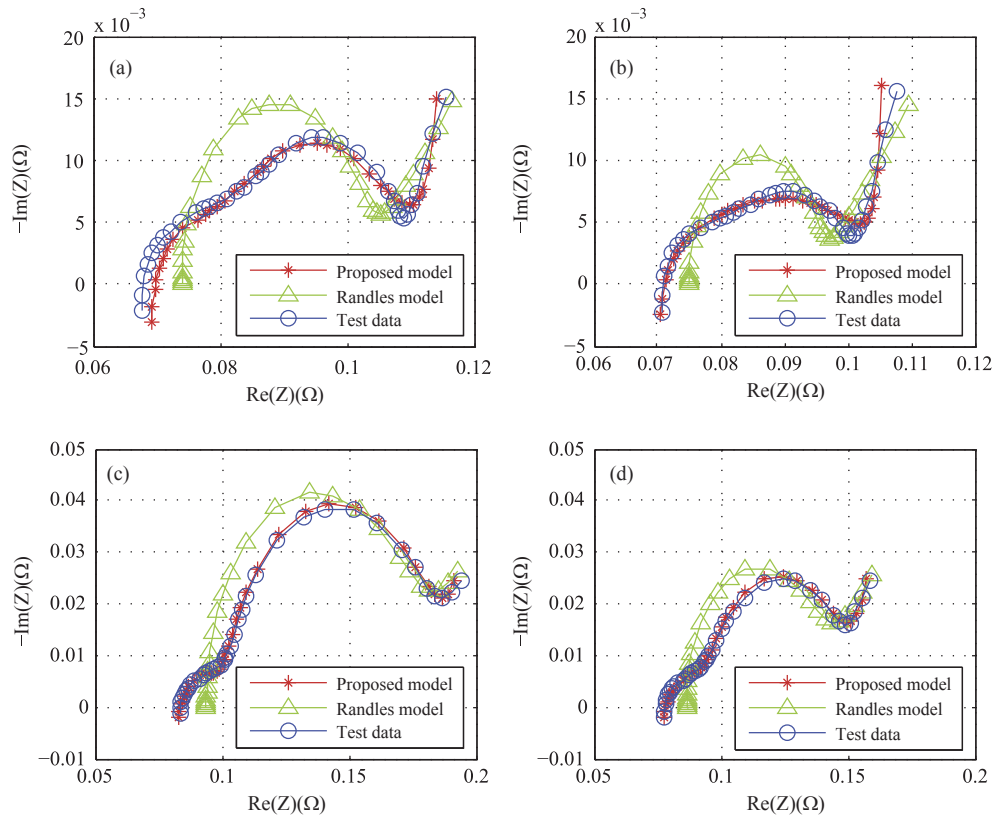

Fig. 8. Fitting results of battery impedance (Cell B) ((a) Cycle 200, fully charged; (b) Cycle 200, half charged; (c) Cycle 800, fully charged; and (d) Cycle 800, half charged).
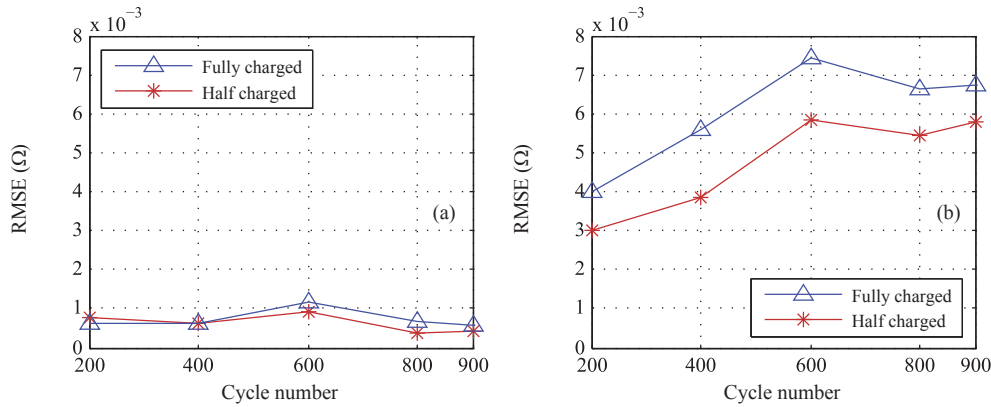
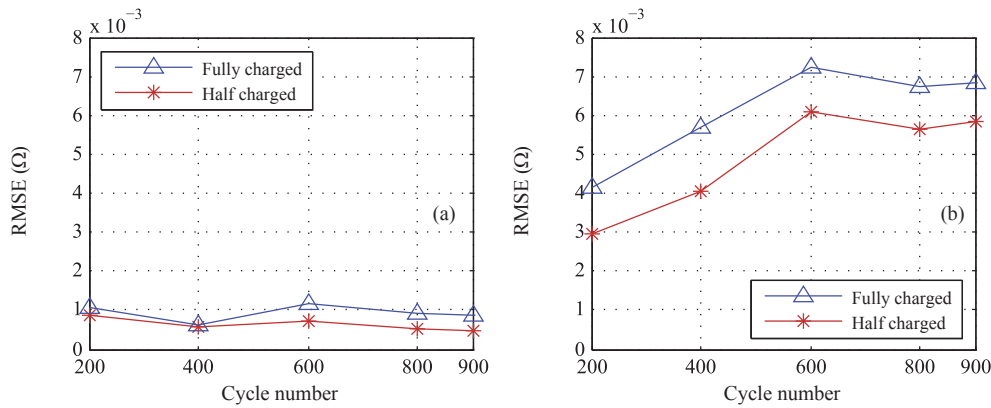**Fig. 9.** Comparison of model accuracy based on RMSE (Cell A) ((a) proposed model; and (b) Randles model).

Fig. 10. Comparison of model accuracy based on RMSE (Cell B) ((a) proposed model; and (b) Randles model).

resistance R_0 is equal to the value at the intersection of the EIS measurement with the real axis [6,22]. Waag et al. argued that the intersection with the real axis contains pure resistors other than R_0 [13]. This phenomenon is supported by our identification results, i.e. the identified R_0 is smaller than the corresponding intersecting value, by comparing Table 4 and Fig. 6(c). With aging from cycle 200 to 900, R_0 of fully charged batteries increases from 62.7 mΩ to 71.8 mΩ, while that of half charged batteries increases from 61.1 mΩ to 73.9 mΩ. This is mainly caused by the decomposition of electrolyte, as described in Ref. [22]. In addition, the pure ohmic resistance of fully charged and half charged batteries is almost identical at the same aging level, implying that the pure ohmic resistance does not vary with SOC, which is also concluded in other publications [13].

As seen in Fig. 12, the SEI film resistance R_{film}/S_n increases with the cycle number. For fully charged state, R_{film}/S_n increases from 2.3 mΩ to 6 mΩ for aging cycle 200–900, almost tripled in amplitude. Meanwhile, R_{film}/S_n increases from 2.8 mΩ to 5.2 mΩ for half

charged cells for aging cycle 200–900, almost doubled in amplitude. It is believed that the growth of anode SEI is a key aging mechanism, leading to battery power and capacity degradation [6,22,34–36]. The film resistance growth can be a measure for predicting capacity and power fade of lithium-ion batteries. The increasing trend of R_{film}/S_n is not as consistent as that of R_0. Moreover, its value is affected by battery SOC levels. The time constant τ_{film} is the product of R_{film} and C_{film}^0. As shown in Fig. 13, the parameter τ_{film} also increases with battery age. It is observed that τ_{film} at half charged state is larger than that at fully charged state.
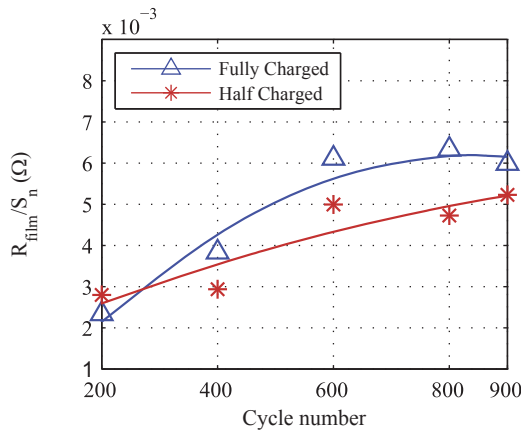
In a lithium-ion battery, the charge-transfer resistance in parallel with the double layer capacitance dominates the depressed semi-ellipse at the mid frequency. In a two-electrode system, it is hard to distinguish the charge-transfer resistances of anode and cathode. Here, the charge-transfer resistance on the cathode side is fixed in order to better demonstrate the aging effects at the anode side. When aging from cycle 200–900, the value of $R_{ct,n}/S_n$(fully

Table 4
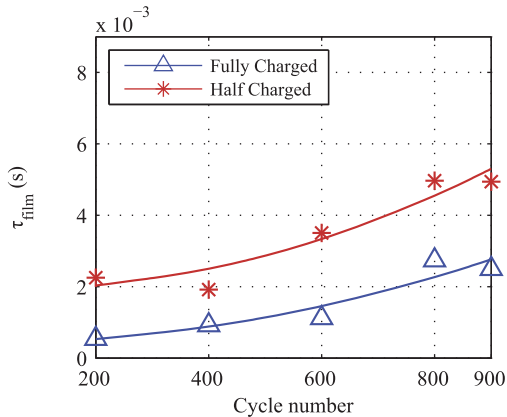Identified parameters vs. cycle number (average of fully charged state).

Cycle Number	R_0 (Ω)	$R_{ct,n}/S_n$(Ω)	R_{film}/S_n(Ω)	τ_{film} (s)	$K_{2,n}$ (s$^{0.5}$)
200	6.27e−02	1.21e−02	2.34e−03	5.38e−04	3.19
400	6.59e−02	3.04e−02	3.84e−03	9.23e−04	3.13
600	6.65e−02	6.46e−02	6.12e−03	1.12e−03	3.01
800	7.18e−02	6.09e−02	6.33e−03	2.74e−03	3.64
900	7.18e−02	7.54e−02	5.99e−03	2.50e−03	3.26

Table 5
Identified parameters vs. cycle number (average of half charged state).

Cycle Number	R_0 (Ω)	$R_{ct,n}/S_n$(Ω)	R_{film}/S_n(Ω)	τ_{film} (s)	$K_{2,n}$ (s$^{0.5}$)
200	6.11e−02	3.20e−03	2.80e−03	2.25e−03	2.45
400	6.52e−02	1.14e−02	2.94e−03	1.92e−03	3.00
600	6.77e−02	3.33e−02	5.00e−03	3.51e−03	2.74
800	6.89e−02	3.48e−02	4.73e−03	4.97e−03	2.86
900	7.39e−02	4.34e−02	5.23e−03	4.94e−03	2.94
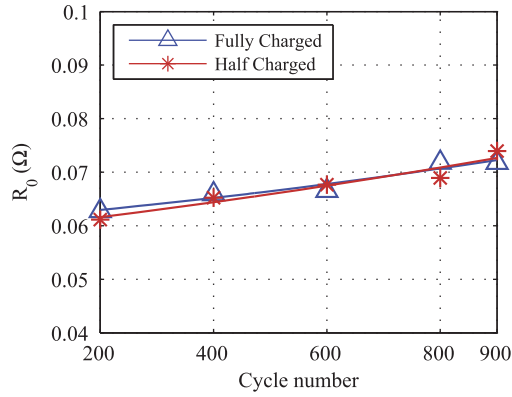
Fig. 11. Pure ohmic resistance R_0 vs. cycle number.
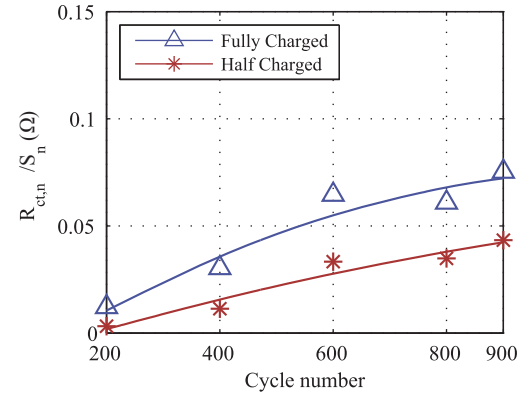
Fig. 14. Anode charge-transfer resistance $R_{ct,n}/S_n$ vs. cycle number.

Fig. 12. SEI resistance R_{film}/S_n vs. cycle number.

The parameter $\tau_{w,n}$, is defined to be equal to the square of lumped parameter $K_{2,n}$ (where n denotes anode):

$$\tau_{w,n} = \left(K_{2,n}\right)^2 = R_n^2/D_{1,n}. \tag{26}$$

From the viewpoint of thermodynamics, $\tau_{w,n}$ represents the time constant of the diffusion dynamics on the anode side. Fig. 15 depicts the relationship between $\tau_{w,n}$ and the aging cycles. It is found that $\tau_{w,n}$ for both half and fully charged batteries show no obvious increasing or decreasing tendency with cycle number. Moreover, $\tau_{w,n}$ of half charged batteries is smaller than that of fully charged battery. A common understanding is that the particle radius keeps constant at different aging and SOC levels. Any change in $\tau_{w,n}$ can be related to that of diffusion coefficient $D_{1,n}$. Therefore, it can be inferred that the diffusion coefficient of half charged batteries is higher than that of fully charged batteries, and battery degradation does not slow down the diffusion dynamics of lithium-ions. Similar summary can be found from Ref. [37] for cathode and Ref. [38] for anode.

6. Conclusion

An electrochemistry-based impedance model is developed to capture the impedance behavior of lithium-ion cells. The modeled dynamics include the charge-transfer reaction at the electrode surface, the diffusion dynamics in the electrodes, the double layer effects, and the resistance/capacitance growth caused by anode insulating film in degradation. In addition, the Nernst equation is directly employed to describe the lithium-ion concentration's effect on open-circuit voltage and a constant phase element is used to
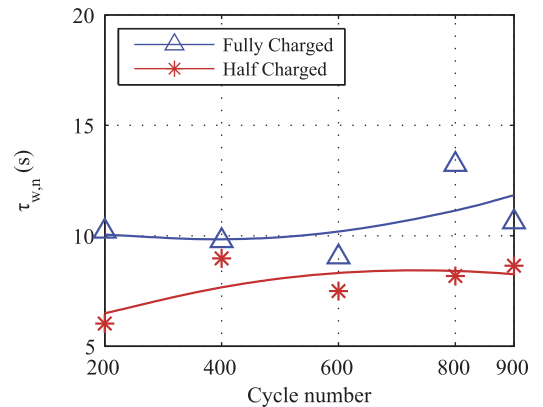
charged) increases from 12.1 mΩ to 75.4 mΩ, almost by 6 times. For half charged state, the value of $R_{ct,n}/S_n$ increases from 3.2 mΩ to 43.4 mΩ. One explanation for this obvious increase is that the SEI film growth reduces charge-transfer reaction rate at the electrode/electrolyte interface. In addition, it is found from Fig. 14 that the charge-transfer resistance at half charged state is smaller than that of fully charged state. This phenomenon can be explained by the change of exchange current density caused by the solid-phase lithium-ion concentrations [29].

Fig. 13. Time constant τ_{film} vs. cycle number.

Fig. 15. Time constant of anode diffusion dynamics vs. cycle number.

better describe the capacitance dispersion caused by electrode porosity. The impedance test results from two lithium-ion battery cells are used to validate the proposed model. The fitting results show that this model works well throughout the aging cycles. Some identified parameters show clear trend as the battery ages, which shows good potential as an indicator for capacity degradation. The charge-transfer resistance and the SEI film resistance demonstrate more significant trend with aging cycles and the results are consistent with experiment-based observations from the literature, which seems to be indicating the potential of the proposed model for battery age estimation.

Acknowledgment

References

[1] J.B. Goodenough, Y. Kim, J. Power Sources 196 (2011) 6688—6694.
[2] S. Chen, M. Wang, J. Ye, J. Cai, Y. Ma, H. Zhou, L. Qi, Nano Res. 6 (2013) 243—252.
[3] M. Safari, C. Delacourt, J. Electrochem. Soc. 158 (2011) A1123—A1135.
[4] P. Liu, J. Wang, J. Hicks-Garner, E. Sherman, S. Soukiazian, M. Verbrugge, H. Tataria, J. Musser, P. Finamore, J. Electrochem. Soc. 157 (2010) A499—A507.
[5] U. Tröltzsch, O. Kanoun, H.-R. Tränkler, Electrochim. Acta 51 (2006) 1664—1672.
[6] Y. Zhang, C.-Y. Wang, X. Tang, J. Power Sources 196 (2011) 1513—1520.
[7] D. Mukoyama, T. Momma, H. Nara, T. Osaka, Chem. Lett. 41 (2012) 444—446.
[8] W.C. Chueh, F. El Gabaly, J.D. Sugar, N.C. Bartelt, A.H. McDaniel, K.R. Fenton, K.R. Zavadil, T. Tyliszczak, W. Lai, K.F. McCarty, Nano Lett. 13 (2013) 866—872.
[9] S. Buller, M. Thele, E. Karden, R.W. De Doncker, J. Power Sources 113 (2003) 422—430.
[10] F. La Mantia, J. Vetter, P. Novák, Electrochim. Acta 53 (2008) 4109—4121.
[11] N. Mellgren, S. Brown, M. Vynnycky, G. Lindbergh, J. Electrochem. Soc. 155 (2008) A304—A319.
[12] D. Dinh Vinh, C. Forgez, K. El-Kadri-Benkara, G. Friedrich, IEEE Trans. Veh. Technol. 58 (2009) 3930—3937.
[13] W. Waag, S. Käbitz, D.U. Sauer, Appl. Energy 102 (2013) 885—897.
[14] A. Eddahech, O. Briat, N. Bertrand, J.-Y. Delétage, J.-M. Vinassa, Int. J. Electr. Power Energy Syst 42 (2012) 487—494.
[15] J.P. Meyers, M. Doyle, R.M. Darling, J. Newman, J. Electrochem. Soc. 147 (2000) 2930—2940.
[16] A.S. Andersson, B. Kalska, L. Häggström, J.O. Thomas, Solid State Ionics 130 (2000) 41—52.
[17] A.S. Andersson, J.O. Thomas, J. Power Sources 97—98 (2001) 498—502.
[18] R.W.J.M. Huang, F. Chung, E.M. Kelder, J. Electrochem. Soc. 153 (2006) A1459—A1465.
[19] G. Sikha, R.E. White, J. Electrochem. Soc. 154 (2007) A43—A54.
[20] G. Sikha, R.E. White, J. Electrochem. Soc. 155 (2008) A893—A902.
[21] D.P. Abraham, S. Kawauchi, D.W. Dees, Electrochim. Acta 53 (2008) 2121—2129.
[22] J. Vetter, P. Novák, M.R. Wagner, C. Veit, K.C. Möller, J.O. Besenhard, M. Winter, M. Wohlfahrt-Mehrens, C. Vogler, A. Hammouche, J. Power Sources 147 (2005) 269—281.
[23] Y. Dai, L. Cai, R.E. White, J. Electrochem. Soc. 160 (2013) A182—A190.
[24] A.M. Colclasure, K.A. Smith, R.J. Kee, Electrochim. Acta 58 (2011) 33—43.
[25] S. Santhanagopalan, Q. Guo, P. Ramadass, R.E. White, J. Power Sources 156 (2006) 620—628.
[26] M. Farkhondeh, C. Delacourt, J. Electrochem. Soc. 159 (2012) A177—A192.
[27] X. Zhang, W. Shyy, A. Marie Sastry, J. Electrochem. Soc. 154 (2007) A910—A916.
[28] A.P. Schmidt, M. Bitzer, Á.W. Imre, L. Guzzella, J. Power Sources 195 (2010) 5071—5080.
[29] G. Ning, B.N. Popov, J. Electrochem. Soc. 151 (2004) A1584—A1591.
[30] S. Santhanagopalan, Q. Guo, R.E. White, J. Electrochem. Soc. 154 (2007) A198—A206.
[31] J.-B. Jorcin, M.E. Orazem, N. Pébère, B. Tribollet, Electrochim. Acta 51 (2006) 1473—1479.
[32] Y. Wang, Z. Cai, Front. Comput. Sci. China 3 (2009) 38—52.
[33] X. Hu, S. Li, H. Peng, J. Power Sources 198 (2012) 359—367.
[34] K. Amine, J. Liu, I. Belharouak, Electrochem. Commun. 7 (2005) 669—673.
[35] H.-H. Chang, H.-C. Wu, N.-L. Wu, Electrochem. Commun. 10 (2008) 1823—1826.
[36] M.B. Pinson, M.Z. Bazant, J. Electrochem. Soc. 160 (2013) A243—A250.
[37] S. Yang, X. Wang, X. Yang, Y. Bai, Z. Liu, H. Shu, Q. Wei, Electrochim. Acta 66 (2012) 88—93.
[38] K. Persson, V.A. Sethuraman, L.J. Hardwick, Y. Hinuma, Y.S. Meng, A. van der Ven, V. Srinivasan, R. Kostecki, G. Ceder, J. Phys. Chem. Lett. 1 (2010) 1176—1180.